Effects of current on wind waves in strong winds

Naohisa Takagaki[1], Naoya Suzuki[2], Yuliya Troitskaya[3], Chiaki Tanaka[2],

Alexander Kandaurov[3], Maxim Vdovin[3]

[1] (Corresponding Author) Department of Mechanical Engineering, University of Hyogo, Shosha 2167, Himeji Hyogo, 671-2280 Japan, *E-mail: takagaki@eng.u-hyogo.ac.jp* Tel/Fax: +81-79-267-47834

[2] Faculty of Science and Engineering, Kindai University, 3-4-1, Kowakae Higashiosaka Osaka, 577-8502 Japan.

[3] Department of Geophysical Research, Institute of Applied Physics, the Russian Academy of Sciences, 46 Ul'yanov Street, Nizhny Novgorod, 603-950, Russia.

Keywords: wind waves, current, Doppler shift

Abstract

It is important to investigate the effects of current on wind waves, called the Doppler shift, both at normal and extreme high wind speeds. Three different types of wind-wave tanks along with a fan and pump are used to demonstrate wind waves and currents in laboratories at Kyoto University, Japan, Kindai University, Japan, and the Institute of Applied Physics, Russian Academy of Sciences, Russia. Profiles of the wind and current velocities and the water-level fluctuation are measured. The wave frequency, wavelength, and phase velocity of the significant waves are calculated, and the water velocities at the water surface and in the bulk of the water are also estimated by the current distribution. The study investigated 27 cases with carrying winds, waves, and currents, at wind speeds ranging from 7 to 67 m s^{-1}. At normal wind speeds under 30 m s^{-1}, wave frequency, wavelength, and phase velocity depend on wind speed and fetch. The effect of the Doppler shift is confirmed at normal wind speeds, i.e., the significant waves are accelerated by the surface current. The phase velocity can be represented as the sum of the surface current and artificial phase velocity, which is estimated by the dispersion relation of the deep-water waves. At extreme high wind speeds, over 30 m s^{-1}, a similar Doppler shift is observed as under the conditions of normal wind speeds. This suggests that the Doppler shift is an adequate model for representing the acceleration of wind

35   waves by current, not only for the wind waves at normal wind speeds but also for those

36   with intensive breaking at extreme high wind speeds. A weakly nonlinear model of

37   surface waves at a shear flow is developed. It is shown that it describes well the

38   dispersion properties of not only small-amplitude waves but also strongly nonlinear and

39   even breaking waves, typical for extreme wind conditions (over 30 m s^{-1}).

40

1. Introduction

42   The oceans flow constantly, depending on the rotation of the Earth, tides, topography,

43   and wind shear. High-speed continuous ocean flows are called currents. Although the

44   mean surface velocity of the ocean is approximately 0.1 m s^{-1}, the maximum current

45   surface velocity is more than 1 m s^{-1} (e.g., Kawabe, 1988; Kelly et al., 2001). The

46   interaction between the current and wind waves generated by wind shear have been

47   investigated in several studies. The acceleration effects of the current on wind waves,

48   called the Doppler shift; the effects of the current on the momentum and heat transfer

49   across the sea surface; and the modeling of waves and currents in the Gulf Stream have

50   been the subject of experimental and numerical investigations (e.g., Dawe and Thompson,

51   2006; Kara et al., 2007; Fan et al., 2009; Shi and Bourassa, 2019). Thus, wind waves

52   follow the dispersion relationship and Doppler shift effect at normal wind speeds.

53   However, these studies were performed at normal wind speeds only, and few studies have

54   been conducted at extreme high wind speeds, for which the threshold velocity is 30 – 35

55   m s^{-1}, representing the regime shift of the air-sea momentum, heat, and mass transport

56   (Powell et al., 2003; Donelan et al., 2004; Takagaki et al., 2012, 2016; Troitskaya et al.,

57   2012, 2020; Iwano et al., 2013; Krall and Jähne, 2014; Komori et al., 2018; Krall et al.,

58   2019). At such extremely high wind speeds, the water surface is intensively broken by

59   the strong wind shear, along with the foam layer, dispersed droplets, and entrained

60   bubbles (e.g. Donelan et al., 2004; Troitskaya et al., 2012, 2017, 2018a, 2018b; Takagaki

61   et al., 2012, 2016; Holthuijsen et al., 2012). It is unclear if the properties of wind waves

62   and the surface foam layer at extremely high wind speeds are similar to those at normal

63   wind speeds. Furthermore, in a hurricane, the local ocean flows may be unusually strong,

64   change rapidly, and strongly affect wind waves. However, the effects of the current on

65   wind waves have not yet been clarified.

66   Therefore, the purpose of this study is to investigate the effects of the current on wind

67   waves in strong winds through the application of three different types of wind-wave tanks,

68   along with a pump.

69
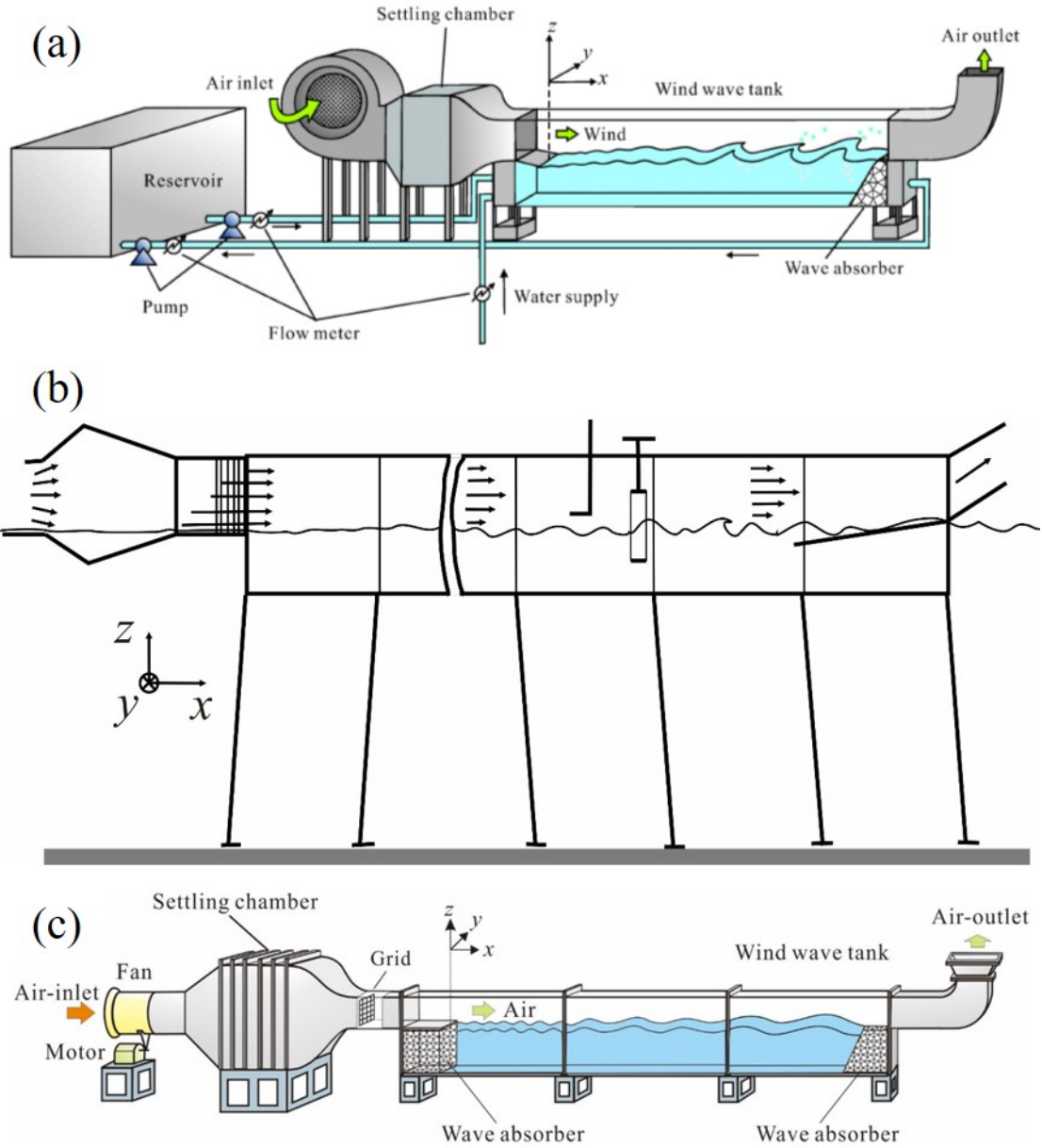
Figure 1. Schematics of wind-wave tanks. (a) High-speed wind-wave tank of Kyoto University. (b) Typhoon simulator of IAP RAS. (c) Wind-wave tank of Kindai University.

2. Experiment

2.1. Equipment and measurement methods

Wind-wave tanks at Kyoto University, Japan and the Institute of Applied Physics, Russian Academy of Sciences (IAP RAS) were used in the experiments (Figs. 1a, 1b). For the tank at Kyoto University, the glass test section was 15 m long, 0.8 m wide, and 1.6 m high. The water depth D was set at 0.8 m. For the tank at IAP RAS, the test section in

the air side was 15 m long, 0.4 m wide, and 0.4 m high. The water depth D was set at 1.5 m. The wind was set to blow over the filtered tap water in these tanks, generating wind waves. The wind speeds ranged from 4.7 to 43 m s^{-1} and from 8.5 to 21 m s^{-1} in the tanks at Kyoto and IAP RAS, respectively. Measurements of the wind speeds, water-level fluctuation, and current were carried out 6.5 m downstream from the edge ($x = 0$ m) in both the Kyoto and IAP RAS tanks. Here, the x, y, and z coordinates are referred to as the streamwise, spanwise, and vertical directions, respectively, with the origin located at the center of the edge of the entrance plate. Additionally, the fetch (x) is defined as the distance between the origin and measurement point ($x = 6.5$ m).

In Kyoto, a laser Doppler anemometer (Dantec Dynamics LDA) and phase Doppler anemometer (Dantec Dynamics PDA) were used to measure the wind velocity fluctuation. A high-power multi-line argon-ion (Ar$^+$) laser (Lexel model 95-7; laser wavelengths of 488.0 and 514.5 nm) with a power of 3 W was used. The Ar$^+$ laser beam was shot through the sidewall (glass) of the tank. Scattered particles with a diameter of approximately 1 μm were produced by a fog generator (Dantec Dynamics F2010 Plus) and were fed into the air flow over the waves (see Takagaki et al. (2012) and Komori et al. (2018) for details). The wind speed values (U_{10}) at a height of 10 m heigh above the ocean and the friction velocity ($u*$) were estimated by the eddy correlation method, by which the mean velocity (U) and the Reynolds stress ($-uv$) in air were measured. The $u*$ was estimated by an eddy correlation method as $u* = (-<uv>)^{1/2}$, because the shear stress at the interface (τ) was defined by $\tau = \rho u*^2 = \rho C_D U_{10}^2$. The value of $(-<uv>)^{1/2}$ was estimated by extrapolating the measured values of the Reynolds stress to the mean surface of $z = 0$ m. The U_{10} was estimated by the log-law: $U_{10} - U_{min} = u*/\kappa \ln(z_{10}/z_{min})$, where U_{min} is the air velocity nearest the water surface (z_{min}) and z_{10} is 10 m. Moreover, the drag coefficient C_D was estimated by $C_D = (u*/U_{10})^2$.

Water level fluctuations were measured using resistance-type wave gauges (Kenek CHT4-HR60BNC) in Kyoto. The resistance wire was placed into the water, and the electrical resistance at the instantaneous water level was recorded at 500 Hz for 600 s using a digital recorder (Sony EX-UT10). The energy of the wind waves (E) was estimated by integrating the spectrum of the water-level fluctuations over the frequency (f). The values of the wavelength (L_S) and phase velocity (C_S) were estimated using the corss-spectrum method (e.g., Takagaki et al., 2017) (see the detail in Appendix). The current was measured using the same LDA system.

In IAP RAS, a hot-wire anemometer (E+E Electrinik EE75) was used to measure the representative mean wind velocity at $x = 0.5$ m and $z = 0.2$ m. The three wind velocities (U_{10}, $u*$, U_∞) at $x = 6.5$ m were taken from Troitskaya et al. (2012) by a Pitot tube. Here,

117 U_∞ is the freestream wind speed. The u^* was estimated by a profile method considering
118 the profiles in the constant flux layer and the wake region:

$$U_\infty - U(z) = u^*\left(-\frac{1}{\kappa}ln(z/\delta) + \alpha\right); \; z/\delta < 0.15, \tag{1}$$

$$U_\infty - U(z) = \beta u^*(1 - z/\delta)^2; \; z/\delta > 0.15, \tag{2}$$

121 respectively. Here, δ is the boundary layer thickness, and α and β are the constant values
122 that depend on flow fields and are calibrated at low wind speeds without the dispersed
123 droplets. At extremely high wind speeds, measuring the profile in the constant flux layer
124 (Eq. 1) is difficult because of the large waves; thus, using β measured at low wind speeds,
125 u^* is estimated by Eq. (2). The value of U_{10} is estimated by Eq. (1) at $z_{10} = 10$ m with
126 measured α at normal wind speeds. The value of C_D is estimated by $C_D = (u^*/U_{10})^2$.
127 Although the measurement methods for u^*, U_{10}, and C_D in IAP RAS and Kyoto are
128 different, the values approximately correspond to each other (see Troitskaya et al. (2012)
129 and Takagaki et al. (2012)).
130   The water-level fluctuations were measured using three handmade capacitive-type
131 wave gauges in IAP RAS. Three wires formed a triangle with 25 mm on a side
132 (x-directional distance between wires Δx is 21.7 mm). The wires were placed in the water,
133 and the output voltages at the instantaneous water level were recorded at 200 Hz for 5400
134 s using a digital recorder through an AD converter (L-Card E14-140). The values (E, f_m,
135 H_S, T_S, C_S, and L_S) were estimated by the same mannar as in Kyoto tank. The current was
136 measured through acoustic Doppler velocimetry (Nortec AS) at $x = 6.5$ m and $z = -10$,
137 -30, -50, -100, -150, -220, and -380 mm (see Troitskaya et al. (2012) for details).
138
2.2. Artificial current experiments at Kindai University
140   Additional experiments were performed using a wind-wave tank at Kindai
141 University with a glass test section 6.5 m long, 0.3 m wide, and 0.8 m high (Fig. 1c) (e.g.
142 Takagaki et al., 2020). The water depth D was set at 0.49 m. A Pitot tube (Okano Works,
143 LK-0) and differential manometers (Delta Ohm HD402T) were used to measure the mean
144 wind velocity. The values of u^*, U_{10}, and C_D (Cases 21-27) were estimated using U_∞ by
145 the empirical curve by Iwano et al. (2013), which was proposed by the eddy correlation
146 method used in Kyoto (see section 2.1).
147   The water level fluctuations were measured using resistance-type wave gauges
148 (Kenek CHT4-HR60BNC). To measure L_S and C_S, another wave gauge was fixed
149 downstream at $\Delta x = 0.02$ m, where Δx is the interval between the two wave gauges. The
150 values (E, f_m, H_S, T_S, C_S, and L_S) were estimated by the same mannar as in Kyoto tank.
151 The current was then measured through electromagnetic velocimetry (Kenek LP3100)

152 with a probe (Kenek LPT-200-09PS) at $x = 4.0$ m. The probe sensing station was 22 mm

153 long with a diameter of 9 mm. The measurements were performed at $z = -15$ to -315 mm

154 at 30 mm intervals. The sampling frequency was 8 Hz, and the sampling time was 180 s.

155

156 **3. Results and discussion**

157 **3.1. Waves and current**

158   Figure 2 shows the vertical distributions of the streamwise water velocity. The

159 water velocities in the three different wind-wave tanks at Kyoto University, Kindai

160 University, and IAP RAS are separately shown in each subfigure. In Fig. 2a, the bulk

161 velocity of water U_{BULK} shows negative values ($U_{BULK} = -0.16$ to -0.01 m s^{-1}) at Kyoto

162 University, which is generated as the counterflow against the Stokes drift at the wavy

163 water surface. In Fig. 2b, the bulk velocity of water demonstrates positive values (U_{BULK}

164 $= 0.019$ to 0.044 m/s) at IAP RAS, because the wind-wave flume is submerged; thus, the

165 Stokes drift on the wavy water surface does not provide the counterflow for the bulk

166 water, unlike in the closed tank at Kyoto University. From Fig. 2c, it is clear that the bulk

167 velocities of the water vary in each case at Kindai University with the use of the pump.

168 Furthermore, the water bulk velocities change from negative to positive ($U_{BULK} = -0.13$

169 to -0.17 m s^{-1}). The bulk velocities of water were defined as the mean velocity with $z =$

170 -0.4 to -0.25 m (see dotted lines in Fig. 2), and the velocities are listed in Table 1.

171 Experiments were performed under 27 different conditions, with the bulk velocity of

172 water provided in the three different wind-wave tanks. The surface velocities of water,

173 U_{SURF}, also varied in the three tanks with respect to wind speed (see Fig. 2). The U_{SURF}

174 values were estimated by the linear extrapolation lines (dashed lines) as the water velocity

175 at the surface ($z = 0$ m) shown in Fig. 2, and the velocities are listed in Table 1.

176   Figure 3 shows the wind-velocity dependency of the wave frequency f_m,

177 wavelength L_S, phase velocity C_S, surface velocity of water U_{SURF}, and bulk velocity of

178 water U_{BULK}. From Figs. 3a–3c, it is clear that both the Kyoto and IAP RAS data

179 demonstrate that the wind waves develop with wind shear. Although f_m in both cases

180 correspond to each other, L_S and C_S in IAP RAS are different from those in Kyoto. The

181 disagreement might be caused by the difference in the wind-wave development or

182 Doppler effect; this is discussed below. From Figs. 3d and 3e, U_{SURF} and U_{BULK} increase

183 with an increase in U_{10} in IAP RAS. However, in Kyoto, U_{SURF} increases, but U_{BULK}

184 decreases with an increase in U_{10}. Moreover, U_{SURF} in IAP RAS corresponds to U_{SURF} in

185 Kyoto. This is because the Stokes drift generated by the wind waves, rather than the

186 current, is significant. For the Kindai data, although f_m, U_{SURF}, and U_{BULK} vary, L_S and C_S

187 are concentrated at single points at $L_S = 0.1$ m and $C_S = 0.4$ m s^{-1}, respectively.
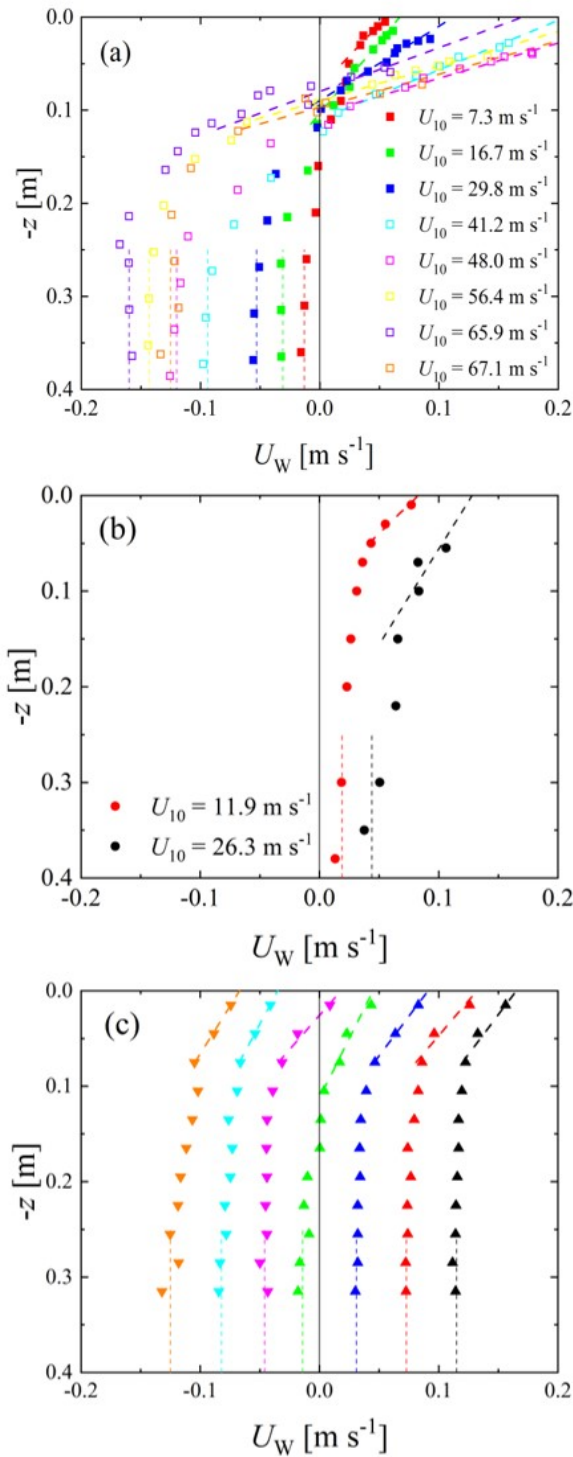
188

189 **Figure 2.** Vertical distributions of water-flow velocity; (a) Kyoto University, (b) IAP RAS, and (c)

190 Kindai University. In (c), plots indicate cases 21–27 starting from right. Dotted and dashed lines

191 indicate the lines used to estimate U_{BULK} and U_{SURF}, respectively. Open symbols show the

192 high-wind-speed cases.

193   **TABLE 1.** Wind and wind-wave properties. F: fetch; N_{PUMP}: pump inverter frequency; U_∞:

194   freestream wind speed; u^*: friction velocity of air; U_{10}: wind speed at 10 m above the sea surface;

195   U_{SURF}: surface flow velocity of water; U_{BULK}: bulk flow velocity of water; C_D: drag coefficient; H_S:

196   significant wave height; T_S: significant wave period; E: wave energy; f_m: significant frequency; C_S:

197   phase velocity; L_S: significant wave length; $C_{S\text{-theor-l}}$: phase velocity predicted by theoretical linear

198   model; $C_{S\text{-theor-nl}}$: phase velocity predicted by theoretical nonlinear model. The values of u^*, U_{10}, and

199   C_D in Kindai were estimated using the empirical curves by Iwano et al. (2013) from U_∞. Superscripts †

200   and †† indicate the artificial following and opposing flows, respectively.

Case	Facility	F [m]	N_{pump} [Hz]	U_∞ [m s⁻¹]	u^* [m s⁻¹]	U_{10} [m s⁻¹]	U_{SURF} [m s⁻¹]	U_{BULK} [m s⁻¹]	C_D [×10⁻³]	H_s [m]	T_s [m]	$E^{0.5}$ [m]	f_m [Hz]	C_s [m s⁻¹]	L_s [m]	$C_{s\text{-theor-l}}$ [m s⁻¹]	$C_{s\text{-theor-nl}}$ [m s⁻¹]
1	Kyoto	6.5	-	4.7	0.24	7.3	0.056	-0.01	1.1	0.0035	0.15	0.00092	6.63	0.40	0.06	0.369	0.374
2	Kyoto	6.5	-	7.2	0.43	11.5	-	-	1.4	0.0131	0.25	0.00353	3.95	0.59	0.16	-	-
3	Kyoto	6.5	-	10.3	0.67	16.7	0.067	-0.031	1.6	0.0231	0.32	0.00624	3.03	0.69	0.23	0.658	0.690
4	Kyoto	6.5	-	12.6	0.89	21.5	-	-	1.7	0.0357	0.39	0.00968	2.59	0.92	0.38	-	-
5	Kyoto	6.5	-	16.3	1.49	29.8	0.112	-0.053	2.5	0.0584	0.50	0.01570	2.01	1.09	0.52	0.972	1.044
6	Kyoto	6.5	-	18.8	1.70	33.6	-	-	2.5	0.0626	0.52	0.01691	1.89	1.18	0.60	-	-
7	Kyoto	6.5	-	22.2	2.08	41.2	0.206	-0.094	2.6	0.0631	0.53	0.01735	1.86	1.35	0.74	1.188	1.258
8	Kyoto	6.5	-	24.8	-	-	-	-	-	0.0668	0.55	0.01866	1.76	1.41	0.79	-	-
9	Kyoto	6.5	-	28.5	2.36	48.0	0.273	-0.120	2.4	0.0727	0.58	0.02058	1.68	1.54	0.93	1.325	1.424
10	Kyoto	6.5	-	31.1	-	-	-	-	-	0.0807	0.62	0.02309	1.58	1.60	1.07	-	-
11	Kyoto	6.5	-	34.8	2.69	56.4	0.241	-0.143	2.3	0.0944	0.68	0.02715	1.44	1.64	1.10	1.379	1.550
12	Kyoto	6.5	-	37.1	2.89	57.7	-	-	2.5	0.1043	0.73	0.03027	1.37	1.76	1.31	-	-
13	Kyoto	6.5	-	39.6	3.38	65.9	0.170	-0.160	2.6	0.1214	0.80	0.03553	1.20	1.84	1.51	1.531	1.694
14	Kyoto	6.5	-	43.3	3.31	67.1	0.272	-0.125	2.4	0.1609	0.93	0.04766	1.08	2.01	1.92	1.743	2.149
15	IAP RAS	6.5	-	8.5	0.40	11.9	0.083	0.019	1.1	0.0214	0.31	0.0056	3.14	0.78	0.25	0.690	0.715
16	IAP RAS	6.5	-	11.0	0.60	16.7	-	-	1.3	0.0305	0.36	0.0081	2.84	0.89	0.32	-	-
17	IAP RAS	6.5	-	13.5	0.90	21.9	-	-	1.7	0.0455	0.43	0.0121	2.41	1.07	0.45	-	-
18	IAP RAS	6.5	-	16.3	1.15	26.3	0.128	0.044	1.9	0.0790	0.50	0.0161	1.95	1.27	0.65	1.111	1.190
19	IAP RAS	6.5	-	18.9	1.50	32.5	-	-	2.1	0.0690	0.54	0.0246	1.85	1.37	0.74	-	-
20	IAP RAS	6.5	-	21.2	1.70	36.9	-	-	2.1	0.0847	0.60	0.0305	1.61	1.61	1.00	-	-
21	Kindai	4.0	15†	5.8	0.28	7.9	0.165	0.115	1.2	0.0044	0.14	0.0012	6.92	0.43	0.06	0.484	0.492
22	Kindai	4.0	10†	5.8	0.28	7.9	0.132	0.073	1.2	0.0050	0.16	0.0014	6.10	0.43	0.07	0.501	0.510
23	Kindai	4.0	5†	5.8	0.28	7.9	0.091	0.031	1.2	0.0049	0.16	0.0014	6.16	0.38	0.06	0.410	0.420
24	Kindai	4.0	0	5.8	0.28	7.9	0.045	-0.014	1.2	0.0054	0.19	0.0014	5.47	0.38	0.07	0.382	0.393
25	Kindai	4.0	5††	5.8	0.28	7.9	0.018	-0.046	1.2	0.0076	0.23	0.0021	4.25	0.36	0.08	0.384	0.400
26	Kindai	4.0	10††	5.8	0.28	7.9	-0.035	-0.082	1.2	0.0098	0.27	0.0027	3.64	0.35	0.10	0.355	0.375
27	Kindai	4.0	15††	5.8	0.28	7.9	-0.067	-0.125	1.2	0.0125	0.34	0.0035	2.94	0.38	0.13	0.381	0.402

203   This shows that the intensity and direction of the current do not significantly affect L_S and

204   C_S but do affect f_m and U_{SURF}. Thus, this implies that the present artificial current changes

205   the water flow dramatically but does not affect the development of the wind waves.

206   Figure 4 shows the dispersion relation and demonstrates that the Kindai data

207   points depend on the variation in the water velocity of the artificial current. The plots for

208   the Kyoto University and IAP RAS cases at normal wind speeds (solid symbols) are

209   concentrated above the solid curve, showing the dispersion relation of the deep-water

210   waves ($\omega^2 = gk$). Meanwhile, the plots for extreme high wind speeds (open symbols) are
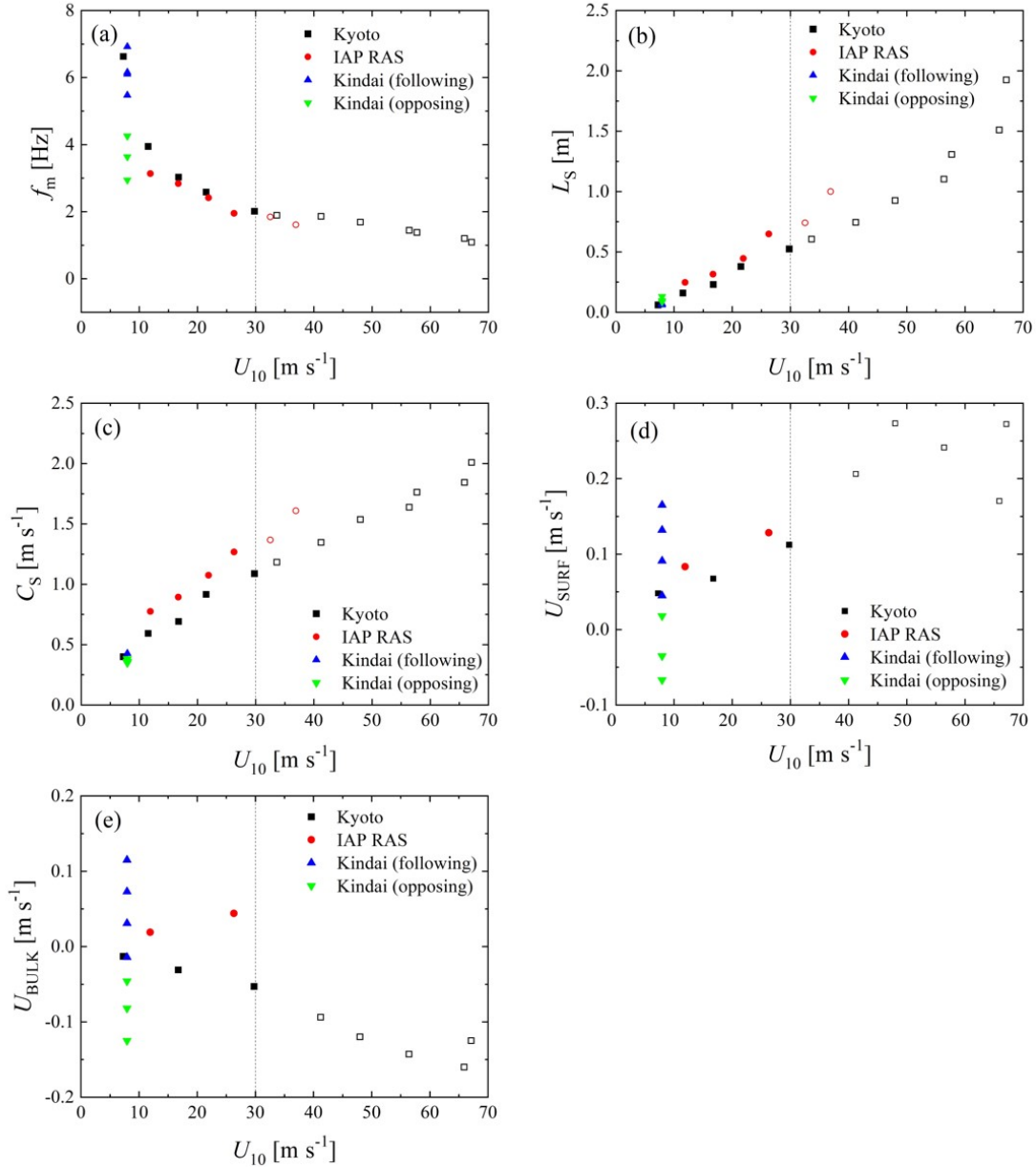
Figure 3. Relationships between U_{10} and (a) significant frequency f_m, (b) significant wave length L_S, (c) phase velocity C_S, (d) surface velocity of water U_{SURF}, and (e) bulk velocity of water U_{BULK}. Open symbols show the high-wind-speed cases.

also concentrated above the solid curve. This implies that the wind waves, along with the intensive breaking at extreme high wind speeds, are dependent on the Doppler shift. To investigate the phase velocity trend, Fig. 5 shows the ratio of the measured phase velocity C_S to the phase velocity $C_{S,0}$ estimated by the dispersion relation of the deep-water waves $(C_{S,0} = (gL_S/2\pi)^{1/2})$ against the wind velocity. From the figure, the ratios at the normal

221
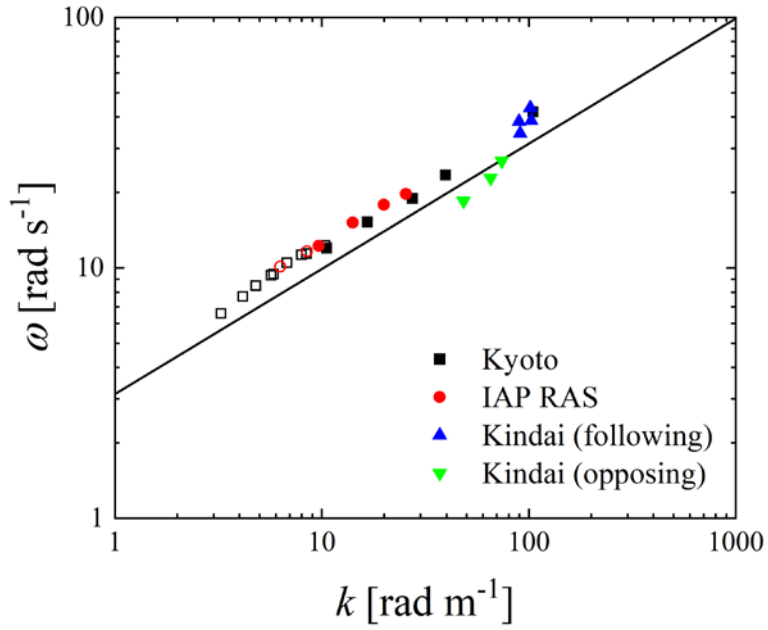
Figure 4. Dispersion relation between angular frequency ω and wave number k. Open symbols show the high-wind-speed cases. Curve shows the dispersion relation of the deep-water waves ($\omega^2 = gk$).

224

225
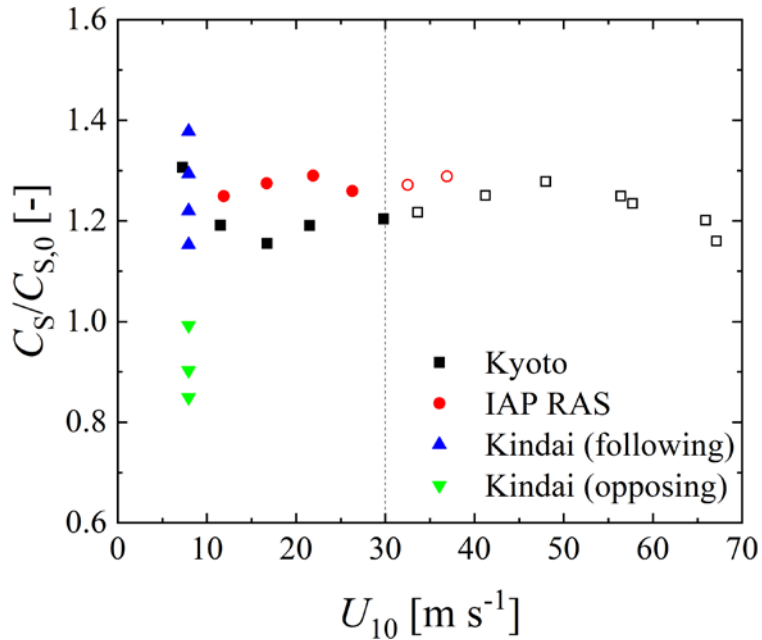
Figure 5. Relationship between the freestream wind speed and phase velocity C_S. The C_S is normalized by phase velocity $C_{S,0}$ without the Doppler effect, estimated by the dispersion relation of the deep-water waves ($C_{S,0} = (gL_S/2\pi)^{1/2}$). Open symbols show the high-wind-speed cases.

229   wind speeds assume a constant value (~1.21 in Kyoto or ~1.27 in IAP RAS). Moreover,
230   the ratios at the extreme high wind speeds take similar values of 1.23 and 1.28 for Kyoto
231   or IAP RAS, respectively. This implies that the phase velocities at extreme high wind
232   speeds are accelerated by the current just as those at normal wind speeds. However, the
233   Kindai values are scattered and increase in the following cases and decrease in the
234   opposing cases. It is clear that the artificial current accelerates (or decelerates) the phase
235   velocity.
236   To interpret the relationship among the measured phase velocity C_S, first phase
237   velocity $C_{S,0}$ estimated by the dispersion relation, and water velocity, two types of phase
238   velocity were evaluated: the sum of $C_{S,0}$ and surface velocity of water U_{SURF} and the sum
239   of $C_{S,0}$ and bulk velocity of water U_{BULK}. Figure 6 shows the relationship between C_S and
240   (a) $C_{S,0} + U_{SURF}$, and (b) $C_{S,0} + U_{BULK}$. In Fig. 6a, we can see that the Doppler shift is
241   confirmed at the normal wind speeds, i.e., the significant waves are accelerated by the
242   surface flow, and the real phase velocity can be represented as the sum of the velocity of
243   the surface flow and the virtual phase velocity, which is estimated by the dispersion
244   relation of the deep-water waves. At extreme high wind speeds over 30 m s^{-1}, a similar
245   Doppler shift is observed as under the conditions of normal wind speeds, as seen in Fig.
246   6a. Meanwhile, in Fig. 6b, although C_S corresponds to $C_{S,0} + U_{BULK}$ at low phase
247   velocities, C_S assumes values larger than $C_{S,0} + U_{BULK}$ at high phase velocities. This
248   suggests that the Doppler shift is an adequate model for representing the acceleration of
249   the wind waves by the current, not only for the wind waves at normal wind speeds but
250   also for those with intensive breaking at extreme high wind speeds. Moreover, the
251   Doppler shift of wind waves occurs due to a very thin surface flow, as the correlation
252   between C_S and $C_{S,0} + U_{SURF}$ is higher than the correlation between C_S and $C_{S,0} + U_{BULK}$.
253
254   **3.2. The theoretical model of waves at the shear flow**
255   The parameters of the observed Doppler shift can be explained more precisely
256   within the theoretical model of the capillary-gravity waves at the surface of the water
257   flows with the velocity profiles prescribed by the experimental data, which are plotted in
258   Fig. 2a–c. Because the dominant wind wave propagates along the wave and water flows,
259   we will consider the 2D-wave model in the 2D flow. This flow is described by the system
260   of 2D Euler equations:

261
$$\frac{\partial u}{\partial t} + u\frac{\partial u}{\partial x} + w\frac{\partial u}{\partial z} + \frac{1}{\rho}\frac{\partial p}{\partial x} = 0, \tag{3}$$

262
$$\frac{\partial w}{\partial t} + u\frac{\partial w}{\partial x} + w\frac{\partial w}{\partial z} + \frac{1}{\rho}\frac{\partial p}{\partial z} = -g,$$

263
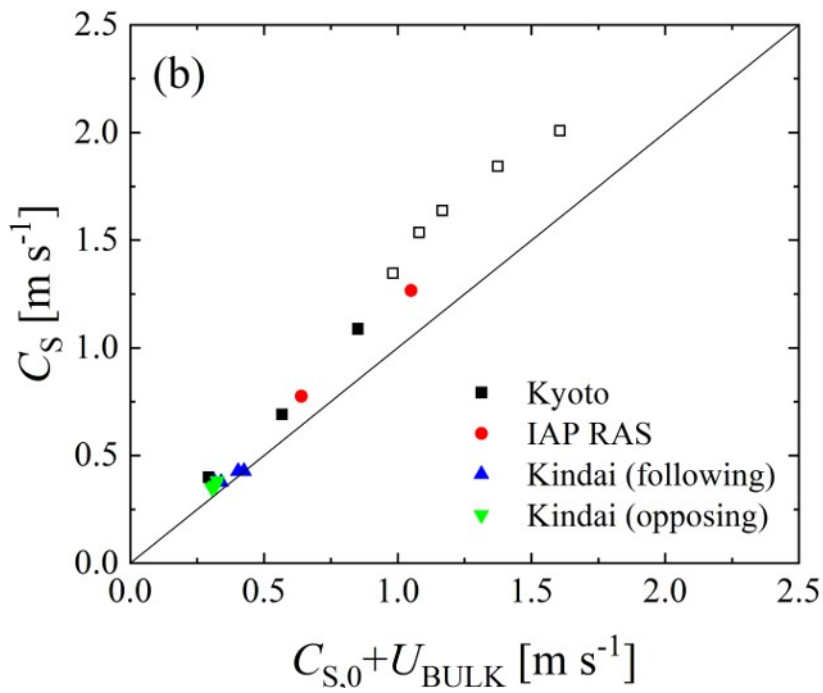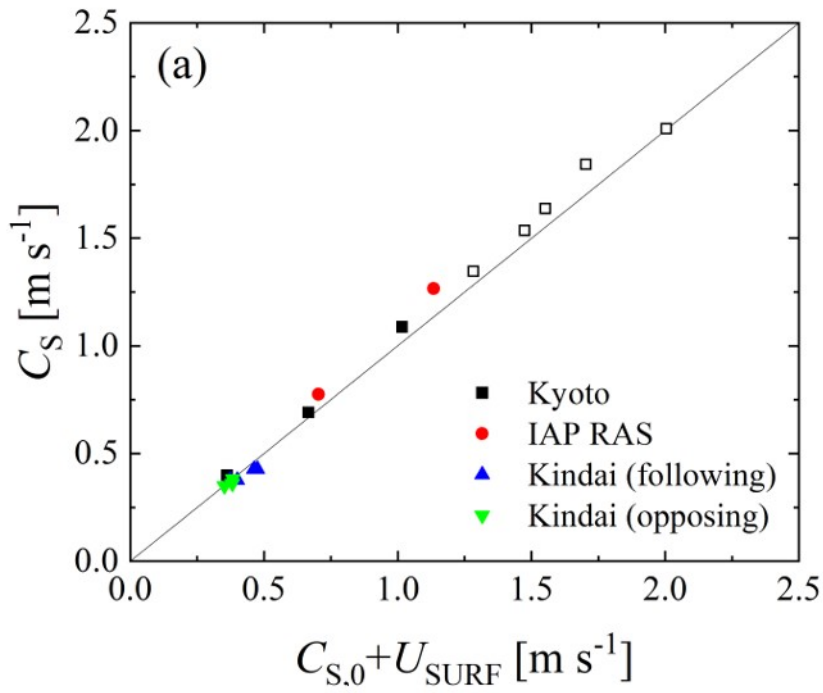
Figure 6. Relationship between phase velocity C_S and (a) sum of $C_{S,0}$ and surface velocity of water U_{SURF}, and (b) sum of $C_{S,0}$ and bulk velocity of water U_{BULK}. Open symbols show the high-wind-speed cases.

267

268 and the condition of non-compressibility:

$$\frac{\partial u}{\partial x} + \frac{\partial w}{\partial z} = 0,$$

269 (4)

270 with the kinematical

$$\frac{\partial \eta}{\partial t} + u\frac{\partial \eta}{\partial x} = w\Big|_{z=\eta(x,t)}$$

271 (5)

272 and dynamical boundary conditions

$$p\Big|_{z=\eta(x,t)} = 0$$

273 (6)

274 at the water surface. Here, u and w are the horizontal and vertical velocity components, p
275 is the water pressure, x and z are the horizontal and upward vertical coordinates, g is the
276 gravity acceleration, and ρ is the water density. The boundary condition at the bottom of

277 the channel is $w\Big|_{z=-D} = 0$. It should be noted that the water depth in almost all the

278 experimental runs exceeded half of the wavelength of the dominant waves (see Table 1).
279 In this case, the deep-water approximation is applicable for describing the surface waves,
280 and the boundary condition of the wave field vanishing with the distance from the water
281 surface can also be used.

282   Because the fluid motion under consideration is 2D, the stream function can be
283 introduced as follows:

$$u = \frac{\partial \psi}{\partial z}; w = -\frac{\partial \psi}{\partial x}.$$

284 (7)

285 To derive the linear dispersion relation for the surface waves at the plane shear flow with
286 the horizontal velocity profile $U_w(z)$, we consider the solution to Eqs. (3, 4) in terms of the
287 stream function as the sum of the undisturbed state with steady shear flow and
288 small-amplitude disturbances. Then, the stream function ψ and pressure p are as follows:

$$\psi(x,z,t) = \int^{z} U_w(z_1)\, dz_1 + \varepsilon \psi_1(x,z,t);$$

289 (8)

$$p(x,z,t) = -\rho g z + \varepsilon p_1(x,z,t),$$

290 (9)

291 where $\varepsilon \ll 1$, and the water elevation value is also the order of ε, namely $\varepsilon \eta_1(x, t)$.

292   In the linear approximation in ε, the system of Eqs. (3, 4) and the boundary
293 conditions of Eqs. (5, 6) take the form:

294
$$\left(\frac{\partial}{\partial t}+\frac{U_w(z)\partial}{\partial x}\right)\left(\frac{\partial^2\psi_1}{\partial x^2}+\frac{\partial^2\psi_1}{\partial z^2}\right)-\frac{\partial\psi_1}{\partial x}\frac{d^2U_w(z)}{dz^2}=0,$$

295
$$\frac{\partial\eta_1}{\partial t}+U_w(0)\frac{\partial\eta_1}{\partial x}=-\left.\frac{\partial\psi_1}{\partial x}\right|_{z=0},$$
(10)

296
$$\left.\frac{\partial p_1}{\partial x}\right|_{z=0}-\rho g\frac{\partial\eta_1}{\partial x}=0,$$

297
$$\left.\psi_1\right|_{z=-D}=0.$$

298   Excluding p_1 with use of the first equation of the system in Eq. (3) and eliminating η_1
299   yields one boundary condition at the water surface for ψ_1:

300
$$\left[\left(\frac{\partial}{\partial t}+\frac{U_w(0)\partial}{\partial x}\right)^2\frac{\partial\psi_1}{\partial z}-\left(\frac{\partial}{\partial t}+U_w(0)\frac{\partial}{\partial x}\right)\frac{\partial\psi_1}{\partial x}\frac{dU_w}{dz}-g\frac{\partial^2\psi_1}{\partial x^2}\right]\Big|_{z=0}=0.$$
(11)

301   For the harmonic wave disturbance, where

302
$$\psi_1(x,z,t)=\Psi(t)\exp(-i(\omega t-kt)),$$
(12)

303   substituting into Eqs. (10, 11) yields the Rayleigh equation for the complex amplitude of
304   the stream function disturbance:

305
$$(\omega-U_w(z)k)\left(\frac{d^2\Psi_1}{dz^2}-k^2\Psi_1\right)+\frac{d^2U_w(z)}{dz^2}k^2\Psi_1=0,$$
(13)

306   with the following boundary condition:

307
$$(\omega-U_w(0)k)^2\frac{d\Psi_1(0)}{dz}+(\omega-U_w(0)k)k\Psi_1(0)\frac{dU_w(0)}{dz}-k^2g\Psi_1(0)=0,$$
(14)

308
$$\left.\Psi_1\right|_{z\to-\infty}\to0.$$

309   Numerically solving the boundary layer problem for Eq. (13) with the boundary
310   conditions in Eq. (14) enables one to obtain the dispersion relation $\omega(k)$ for the surface
311   waves at the inhomogeneous shear flow. Note that because the phase velocity of the
312   waves significantly exceeded the flow velocity in all experiments (cf. Figs. 2 and 3), the
313   Rayleigh equation did not have a singularity, and the calculated frequency and phase
314   velocity of the wave were real values, i.e., the current was neutral stable.
315   The wave phase velocities $C_{S\text{-theor-l}}=\omega(k)/k$ were calculated for the parameters of
316   those experiments that contained complete information about the course and
317   characteristics of the waves, namely 1, 3, 5, 7, 9, 11, 13–15, 18, and 21–27 from Table 1.
318   The results are presented in Fig. 7a as the measured phase velocity C_S versus calculated
319   phase velocity $C_{S\text{-theor-l}}$. One can see that the model corresponds to the data substantially
320   better than does the model of linear potential waves at the homogeneous current U_{BULK}
321   (compare Fig. 6b). Considering the structure of the wave disturbances of the stream
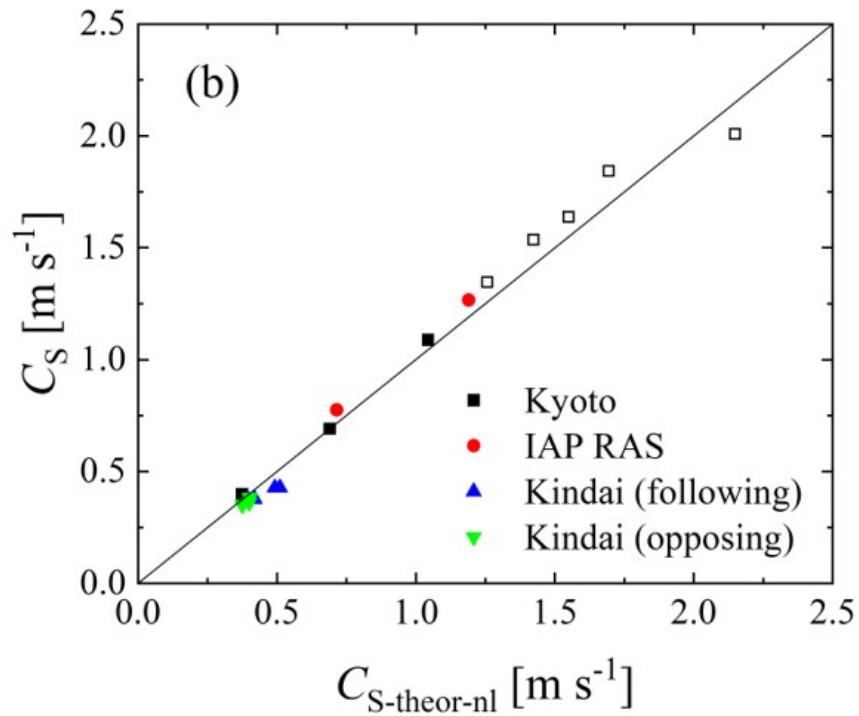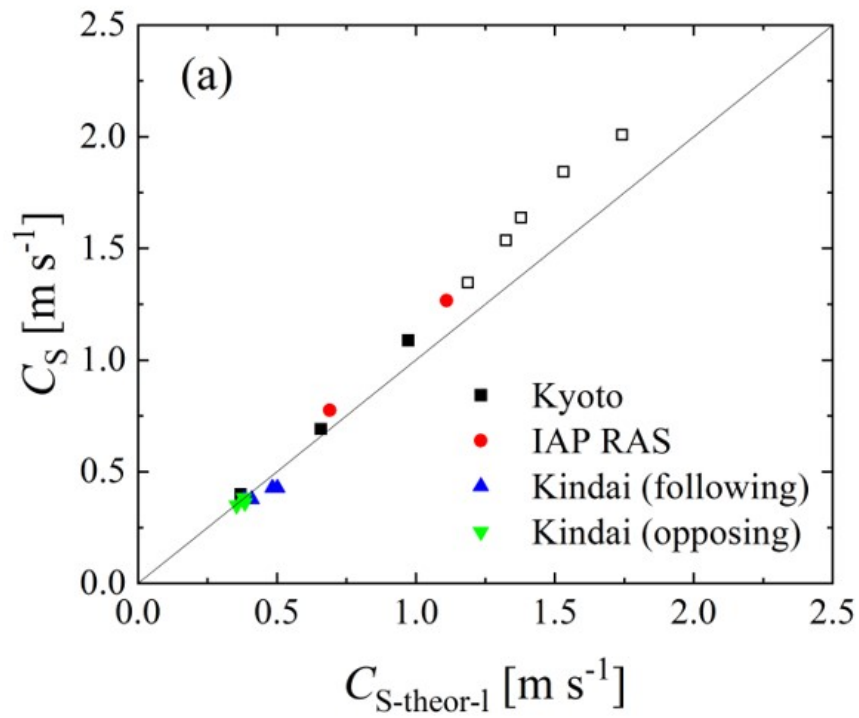
Figure 7. The measured phase velocity C_S versus theoretical prediction: (a) linear model, and (b) nonlinear model.
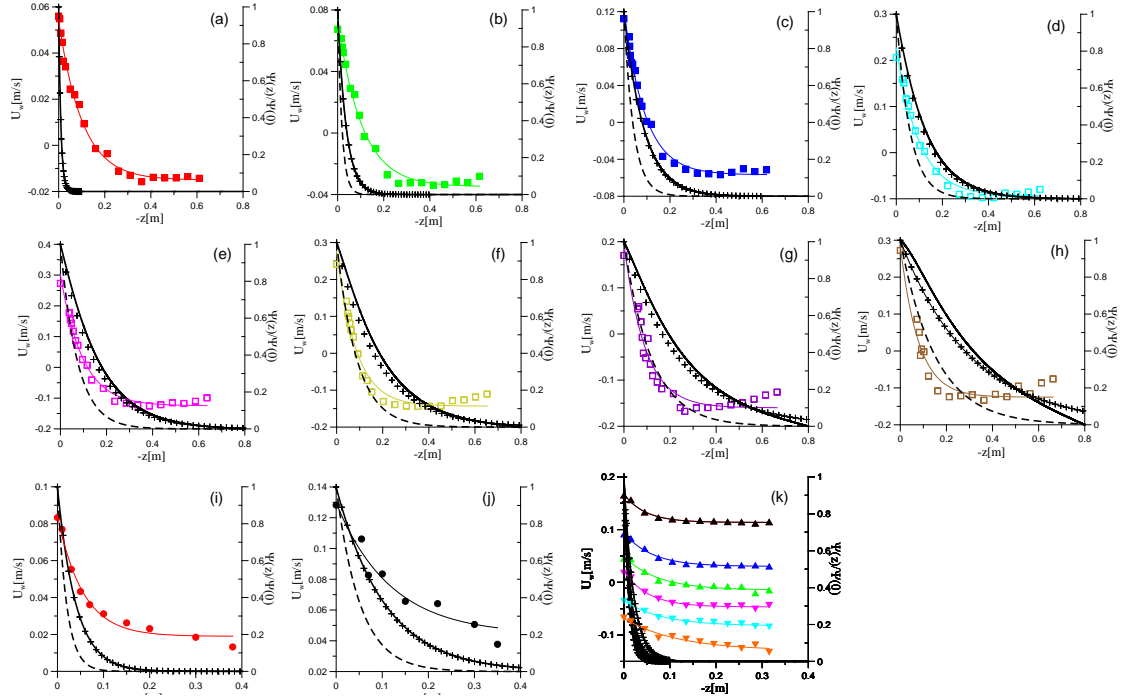
Figure 8. Vertical velocity profiles (points), their fitting (thin color line), the eigenfunction of the Eq. (8) with the boundary conditions Eq. (9) (black solid curve), the function e^{kz} (crosses), the function e^{2kz} (dashed line). The panels (a)-(j) corresponds to the experiments No. 1, 3, 5, 7, 9, 11, 13-15, 18 respectively, the panel (k) corresponds to the experiments No. 21-27.

function, $\Psi_1(z)$, which was found as the eigenfunction of the boundary problem of Eqs. (11, 12). The profiles of $\Psi_1(z)$ are presented in Fig. 8. One can see that in all cases the functions $\Psi_1(z)$ are close to e^{kz} at the background of the mean velocity profiles. Moreover, for experiments No. 1, 3, 5, 15, and 21–27 (see Fig. 8a, 8b, 8c, 8i, and 8k), the wave field is concentrated near the surface at a distance less than the scale of the change in the mean flow, where the flow velocity is approximately equal to U_{SURF}. This explains the good correlation in these cases of the observed phase velocity with the phase velocity of waves at the homogeneous current U_{SURF} presented in Fig. 6a. At the same time, for experiments No. 7, 9, 5, 11, 13, 14, and 18 (see Figs. 8d–8h, and 8j), the scale of the variability of the flow is significantly smaller than the scale of the wave field. Under these conditions, a significant difference between the phase velocity of the waves and that given by the linear dispersion relation can be due to the influence of nonlinearity.

To estimate the nonlinear addition to the wave phase velocity, we used the results of the weakly nonlinear theory of surface waves for the current with a constant shear. Of course, the flow in the experiments of the present work does not have a constant shift, and this was considered when obtaining the linear dispersion relation. However, it should be

348   taken into account that the contributions of the *n*-th harmonic to the nonlinear dispersion
349   relation are determined by wave fields in the *n*-power, which have a scale that is *n* time
350   smaller than the first harmonic. Additionally, the model of constant shear of the mean
351   current velocity is already approximately applicable for the 2nd harmonic (see Fig. 8).

352   We use the nonlinear dispersion relation for waves in the current with a constant
353   shift in the deep-water approximation, which was obtained by Simmen and Saffman
354   (1985):

$$(\omega - U_w(0)k)^2 \frac{d\Psi_1(0)}{dz} + (\omega - U_w(0)k)k\Psi_1(0)\frac{dU_w(0)}{dz} - k^2 g\Psi_1(0) = \gamma(ka)^2,$$

$$\gamma = \frac{(\omega_0 - U_w(0)k)^2}{2k}\left(1 - \frac{1}{2}\Omega^2 + \left(1 + 2\Omega + \frac{1}{2}\Omega^2\right)^2\right),$$ (15)

$$\Omega = \frac{1}{(\omega_0 - U_w(0)k)}\frac{dU_w(0)}{dz},$$

358   Here, ω_0 is the solution of the linear dispersion equation. Eq. (15) is rewritten in the
359   notation of this work and formulated in a reference frame in which the surface of the
360   water has the velocity $U_w(0)$. Note that the linear part of Eq. (15) coincides with Eq. (14).
361   The results of solving Eq. (15) are presented in Fig. 7b similarly to Fig. 7a as the
362   measured phase velocity C_S versus calculated phase velocity $C_{S\text{-theor-nl}} = \omega(k)/k$, where
363   one can see their good agreement with each other. Thus, the wave frequency shift can be
364   explained by two factors, including the Doppler shift at the mean flow and the nonlinear
365   frequency shift, while, the latter can also be interpreted in its physical nature as the wave
366   frequency shift in the presence of its orbital velocities.

367   Recent studies have indicated a regime shift in the momentum, heat, and mass
368   transfer across an intensive broken wave surface along with the amount of dispersed
369   droplets and entrained bubbles at extreme high wind speeds over 30 m s^{-1} (e.g., Powell et
370   al., 2003; Donelan et al., 2004; Takagaki et al., 2012, 2016; Troitskaya et al., 2012; Iwano
371   et al., 2013; Krall and Jähne, 2014; Komori et al., 2018; Krall et al., 2019). Thus, there is
372   the possibility of a similar regime shift in the Doppler shift of wind waves by the current
373   at extreme high wind speeds. However, the present study reveals that such a Doppler shift
374   is observed as under the conditions of normal wind speeds. In this case, the weakly
375   nonlinear approximation turns out to be applicable for describing the dispersion
376   properties of not only small-amplitude waves but also nonlinear and even breaking waves.
377   This implies that the intensive wave breaking at extreme high wind speeds occurs with
378   the saturation (or dumping) of the wave height rather than the wavelength. This evidence
379   might be helpful in investigating and modelling the wind-wave development at extreme
380   high wind speeds.

381

4. Conclusion

The effects of the current on wind waves were investigated through laboratory experiments in three different wind-wave tanks with a pump at Kyoto University, Japan, Kindai University, Japan, and IAP RAS. The study investigated 27 cases with carrying winds, waves, and currents, at wind speeds ranging from 7–67 m s^{-1}. We observed that the wind waves do not follow the dispersion relation in either the normal or the extremely high wind speeds in the three tanks (Fig. 4)—excluding case 25, in which the artificial current experiment used the Kindai tank. In case 25, U_{SURF} is approximately zero (Fig. 3); thus, the Doppler shift does not occur. Then, using 18 datasets (Kyoto and IAP RAS tanks) (Fig. 5), we found that the ratio of $C_{\mathrm{S}}/C_{\mathrm{S},0}$ is constant at both normal and extremely high wind speeds. Moreover, in the artificial current experiment in Kindai, we observed that the ratio varies (Fig. 5). The evidence from the three tank experiments implies that the same wave-current interaction occurs at normal and extremely high wind speeds.

To develop an adequate model for wave-current interaction at normal and extremely high wind speeds, we validated four models (Figs. 6 and 7). At normal wind speeds under 30 m s^{-1}, the wave frequency, wavelength, phase velocity of waves, and surface velocity of the water depended on the wind speed (Fig. 3). However, the bulk velocity of the water showed a dependence on the tank type, i.e., a large tank with a submerged wind-wave flume (IAP RAS) or wind flume above a tank (general type of wind-wave tank) (Kyoto University) (Fig. 3). The effect of the Doppler shift was confirmed at normal wind speeds, i.e., the significant waves were accelerated by the surface flow, and the phase velocity was represented as the sum of the surface velocity of water and the phase velocity, which is estimated by the dispersion relation of the deep-water waves (Fig. 6). At extreme high wind speeds over 30 m s^{-1}, a Doppler shift was observed similar to that under the conditions of normal wind speeds (Figs. 4 and 5). This suggests that the Doppler shift is an adequate model for representing the acceleration of wind waves by the current, not only for the wind waves at normal wind speeds but also for those with intensive breaking at extreme high wind speeds. The data obtained by the artificial current experiments conducted at Kindai University were used to explain how the artificial current accelerates (or decelerates) the significant waves. A weakly nonlinear model of surface waves at a shear flow was developed (Fig. 7). It was shown that it describes well the dispersion properties of not only small-amplitude waves but also strongly nonlinear and even breaking waves, typical for extreme wind conditions, with speeds, U_{10}, exceeding 30 m s^{-1}.

416

Data availability

All analytical data used in this study are compiled in Table 1.

Author contributions

NT and NS planned the experiments, evaluated the data, and contributed equally to writing the paper excluding Section 3.2. YT planed the Russia experiment, provided the linear and non-linear models, prepared figures in Section 3.2, and contributed to writing Section 3.2. CT prepared all figures excluding Section 3.2. NT performed the wind, current, and wave measurements in the Kyoto experiment. NT, NS, and CT performed the wind, current, and wave measurements in the Kindai experiment. AK and MV performed the wind, current, and wave measurements in the Russia experiment.

Competing interests

The authors declare that they have no conflict of interest.

Acknowledgements

This work was supported by the Ministry of Education, Culture, Sports, Science and Technology (Grant-in-Aid No's. 18H01284, 18K03953, and 19KK0087). This project was supported by the Japan Society for the Promotion of Science and the Russian Foundation for Basic Research (grant 18-55-50005, 19-05-00249, 20-05-00322) under the Japan-Russia Research Cooperative Program. The experiments of IAP RAS were partially supported by RSF (project 19-17-00209). We thank Prof. S. Komori and Mr. Tsuji for their help in conducting the experiments and for useful discussions. The experiments of IAP RAS were performed at the Unique Scientific Facility "Complex of Large-Scale Geophysical Facilities" (http://www.ckp-rf.ru/usu/77738/).

Appendix

It is important to estimate the phase velocity and wavelength of the significant wind-waves using the water-level fluctuation data. Here, we explain the method, called as the cross-spectrum method. The water-level fluctuation $\eta(x, t)$ at arbitral location x and time t is shown as the equation:

$$\eta(x,t) = \int_{-\Omega}^{\Omega} A(\omega) e^{i(\omega t - k(\omega)x)} d\omega \tag{A1}$$

where ω is the angular frequency, $A(\omega)$ is the complex amplitude, and $k(\omega)$ is the

452 wavenumber of waves having ω, Ω is the maximum angular frequency of the surface

453 waves. $F_\eta(\omega)$ is the Fourier transformation of $\eta(x, t)$ when the measurement time t_m and Ω

454 are sufficiently large. Using the inverse Fourier transformation of $F_\eta(\omega)$, $\eta(x, t)$ is shown

455 as:

$$\eta(x,t) = \frac{1}{2\pi} \int_{-\Omega}^{\Omega} F_\eta(\omega)e^{i\omega t}d\omega. \tag{A2}$$

456

457 Comparing Eqs. (A1, A2), $F_\eta(\omega)$ is $F_\eta(\omega) = 2\pi A(\omega)e^{-ik(\omega)x}$. Assuming that the wind waves

458 change the shape little between two wave probes set upstream and downstream, we can

459 set the upstream and downstream water-level fluctuations $\eta_1(t) = \eta(0, t)$ and $\eta_2(t) = \eta(\Delta x,$

460 $t)$, respectively, with Δx downstream from the first probe. The Fourier transformations

461 $F_{\eta 1}(\omega)$ and $F_{\eta 2}(\omega)$ for $\eta_1(t)$ and $\eta_2(t)$, respectively, are shown as:

$$F_{\eta_1}(\omega) = 2\pi A(\omega), \tag{A3}$$

$$F_{\eta_2}(\omega) = 2\pi A(\omega)e^{-ik(\omega)\Delta x}. \tag{A4}$$

464 Then, the power spectra $S_{\eta 1\eta 1}(\omega)$ and $S_{\eta 2\eta 2}(\omega)$ for $\eta_1(t)$ and $\eta_2(t)$, respectively, are shown

465 as:

$$S_{\eta_1\eta_1}(\omega) = \frac{1}{t_m}F_{\eta_1}^*(\omega)F_{\eta_1}(\omega) = \frac{1}{t_m}4\pi^2|A(\omega)|^2, \tag{A5}$$

466

$$S_{\eta_2\eta_2}(\omega) = \frac{1}{t_m}F_{\eta_2}^*(\omega)F_{\eta_2}(\omega) = S_{\eta_1\eta_1}(\omega). \tag{A6}$$

467

468 Here, the superscript * indicates the complex conjugate number. The cross-spectrum

469 $Cr(\omega)$ for $\eta_1(t)$ and $\eta_2(t)$ is shown as:

$$Cr(\omega) = \frac{1}{t_m}F_{\eta 1}^*(\omega)F_{\eta 2}(\omega) = \frac{1}{t_m}4\pi^2|A(\omega)|^2e^{ik(\omega)\Delta x}. \tag{A7}$$

470

471 Using Euler's theorem, Eq. (A7) transforms to:

$$Cr(\omega) = \frac{1}{t_m}4\pi^2|A(\omega)|^2(\cos k(\omega)\Delta x + i\sin k(\omega)\Delta x)$$

472

$$= S_{\eta_1}(\omega)(\cos k(\omega)\Delta x + i\sin k(\omega)\Delta x). \tag{A8}$$

473

474 The cospectrum $Co(\omega)$ and quad spectrum $Q(\omega)$ are defined as the real and imaginary

475 parts of $Cr(\omega)$, respectively, shown as $Cr(\omega) = Co(\omega) + iQ(\omega)$. Moreover, the phase $\theta(\omega)$

476 is defined as $\theta(\omega) = \tan^{-1}(Q(\omega)/Co(\omega))$. Thus, $\theta(\omega)$ can be calculated as:

$$\theta(\omega) = \tan^{-1}(\tan(k(\omega)\Delta x) = k(\omega)\Delta x. \tag{A9}$$

478 Generally, the velocity of the wind waves C is defined as:

$$C = \frac{\omega}{k} = \frac{L}{T}, \tag{A10}$$

479

480 where L is the wavelength and T is the wave period. From Eqs. (A9, A10), $C(\omega)$ and $L(\omega)$

481 can be transformed to

$$C(\omega) = \frac{\omega}{k} = \frac{\omega \Delta x}{\theta(\omega)}, \tag{A11}$$

482

$$L(\omega) = \frac{2\pi}{k} = \frac{2\pi \Delta x}{\theta(\omega)}. \tag{A12}$$

483
484 When we estimate the phase $\theta_m(\omega_m)$ at the angular frequency of significant wind-waves
485 ω_m ($=2\pi f_m$), the phase velocity of the significant wind waves C_S ($= C(\omega_m)$) and significant
486 wavelength L_S ($= L(\omega_m)$) are calculated by:

$$C_S = \frac{2\pi f_m \Delta x}{\theta(f_m)}, \tag{A13}$$

487

$$L_S = \frac{2\pi \Delta x}{\theta(f_m)}. \tag{A14}$$

488

489 In the study, C_S and L_S are estimated by Eqs. (A13, A14) using the cross-spectrum
490 method.

491

492

493 **References**

494 Dawe, J. T., Thompson, L., (2006), Effect of ocean surface currents on wind stress, heat
495   flux, and wind power input to the ocean, Geophysical Research Letters, 33, L09604,
496   doi:10.1029/2006GL025784
497 Donelan, M.A., Haus, B.K., Reul, N., Plant, W.J., Stiassnie, M., Graber, H.C., Brown,
498   O.B., Saltzman, E.S., (2004), On the limiting aerodynamic roughness of the ocean
499   in very strong winds, Geophysical Research Letters, 31,
500   doi:10.1029/2004GL019460. L18306
501 Fan, Y., Ginis, I., Hara, T., (2009), The Effect of Wind–Wave–Current Interaction on
502   Air–Sea Momentum Fluxes and Ocean Response in Tropical Cyclones, Journal of
503   Physical Oceanography, 39, pp. 1019-1034.
504 Iwano, K., Takagaki, N., Kurose, R., Komori, S., (2013), Mass transfer velocity across
505   the breaking air-water interface at extremely high wind speeds, Tellus B 65, 21341,
506   doi:10.3402/tellusb.v65i0.21341
507 Kara, A. B., Metzger, E. J., Bourassa, M. A., (2007), Ocean current and wave effects on
508   wind stress drag coefficient over the global ocean, Geophysical Research Letters,
509   34, L01604, doi:10.1029/2006GL027849

Kawabe, M., (1988), Variability of Kuroshio velocity assessed from the sea-level difference between Naze and Nishinoomote, Journal of oceanographical Society of Japan, 44, pp. 293-304.

Kelly, K. A., Dickinson, S., McPhaden, M. J., Johnson, G. C., (2001), Ocean currents evident in satellite wind data, Geophysical Research Letters, 28(12), pp. 2469-2472.

Komori, S., Iwano, K., Takagaki, N., Onishi, R., Kurose, R., Takahashi, K., Suzuki, N., (2018), Laboratory measurements of heat transfer and drag coefficients at extremely high wind speeds, Journal of Physical Oceanography, doi:10.1175/JPO-D-17-0243.1

Krall, K. E., Jähne, B., (2014), First laboratory study of air-sea gas exchange at hurricane wind speeds, Ocean Science, 10(2), 257-265, doi:10.5194/os-10-257-2014

Krall, K. E., Smith, A. W., Takagaki, N., Jähne, B., (2019), Air–sea gas exchange at wind speeds up to 85 m s-1, Ocean Science, 15(6), doi: 10.5194/os-15-1783-2019

Powell, M. D., Vickery, P. J., Reinhold, T. A., (2003), Reduced drag coefficient for high wind speeds in tropical cyclones, Nature, 422, 279–283, doi:10.1038/nature01481

Shi, Q., Bourassa, M. A., (2019), Coupling Ocean Currents and Waves with Wind Stress over the Gulf Stream, Remote Sensing, 11, 1476, doi:10.3390/rs11121476

Simmen, J. A., Saffman, P. G., (1985), Steady deep-water waves on a linear shear current, Studies in Applied Mathematics, 73, 35–57, doi: 10.1002/sapm198573135

Takagaki, N., Komori, S., Suzuki, N., Iwano, K., Kuramoto, T., Shimada, S., Kurose, R., Takahashi, K., (2012), Strong correlation between the drag coefficient and the shape of the wind sea spectrum over a broad range of wind speeds, Geophysical Research Letters, 39, doi:10.1029/2012GL053988. L23604

Takagaki, N., Komori, S., Suzuki, N., Iwano, K., Kurose, R., (2016), Mechanism of drag coefficient saturation at strong wind speeds, Geophysical Research Letters, 43, doi:10.1002/2016GL070666

Takagaki, N., Komori, S., Ishida, M., Iwano, K., Kurose, R., Suzuki, N., (2017), Loop-type wave-generation method for generating wind waves under long-fetch conditions, Journal of Atmospheric Oceanic Technology, 34(10), 2129–2139, doi:10.1175/JTECH-D-17-0043.1

Takagaki, N., Suzuki, N., Takahata, S., Kumamaru, H., (2020), Effects of air-side freestream turbulence on development of wind waves, Experiments in Fluids, 61, 136, doi:10.1007/s00348-020-02977-9

Troitskaya, Y. I., Sergeev, D. A., Kandaurov, A. A., Baidakov, G. A., Vdovin, M. A., Kazakov, V. I., (2012), Laboratory and theoretical modeling of air-sea momentum

546   transfer under severe wind conditions, Journal of Geophysical Research, 117,

547   C00J21, doi:10.1029/2011JC007778

548 Troitskaya, Y., Sergeev, D., Vdovin, M., Kandaurov, A., Ermakova, O., Takagaki, N.,

549   (2020), Laboratory study of the effect of surface waves on heat and momentum

550   transfer at strong winds, Journal of Geophysical Research Oceans, doi:

551   10.1029/2020JC016276

552

553